CHAPTER W16

Superconductors

W16.1 Further Discussion of Thermal Conductivity in Superconductors

When heat is conducted primarily by the electrons in the normal state for $T > T_c$ (i.e., when $\kappa_n \approx \kappa_{en}$), then below T_c, κ_s falls rapidly below κ_n. This is illustrated in Fig. W16.1*a* for the elemental superconductor Al. In this case $\kappa_s \approx \kappa_{es}$ is observed to approach zero exponentially as T decreases, again providing strong evidence for a superconducting energy gap. When the conduction of heat by phonons dominates in the normal state for $T > T_c$ (i.e., when $\kappa_n \approx \kappa_{ln}$), as is often the case in alloys where electron-impurity scattering effects are important and also in the high-T_c superconductors discussed in Section 16.5 of the textbook,[†] then below T_c, $\kappa_s \approx \kappa_{ls}$. In this case, κ_s can actually be greater than the corresponding normal-state value κ_n, as illustrated in Fig. W16.1*b* for superconducting alloys of Pb with In and Bi. In most cases both the conduction electrons and the phonons make appreciable contributions to the conduction of heat in the normal state above T_c, so the variation of $\kappa_s(T)$ below T_c lies between the two limits presented here.

The situation is more complicated when the superconductor is in the mixed state. The normal electrons associated with the vortices can scatter phonons, thus decreasing κ_{ls}, but can also transport heat, thus increasing κ_{es}.

W16.2 Two-Fluid Model

The *two-fluid model* of Gorter and Casimir[‡] presented in 1934 is a classical thermodynamic treatment which assumes that in the superconducting state the conduction electrons can be separated into two separate, interpenetrating but noninteracting phases or fluids. In this model the concentration of conduction electrons for $T < T_c$ is given by $n = n_s(T) + n_n(T)$, where n_s and n_n are the concentrations of the *superconducting* and *normal* electrons, respectively. The fraction of superconducting electrons is $f_s = n_s/n$, while for the normal electrons, $f_n = n_n/n = 1 - f_s$. It is assumed that both n_s and n_n are temperature dependent, with $n_s(T_c) = n_n(0\ \text{K}) = 0$ and $n_s(0\ \text{K}) = n_n(T_c) = n$.

According to one approach, the superconducting fraction is given by $f_s(T) = 1 - (T/T_c)^4$ and the Gibbs free energy per unit volume of the superconducting state is

[†] The material on this home page is supplemental to *The Physics and Chemistry of Materials* by Joel I. Gersten and Frederick W. Smith. Cross-references to material herein are prefixed by a "W"; cross-references to material in the textbook appear without the "W."

[‡] C. J. Gorter and H. B. G Casimir, *Physica*, **1**, 306 (1934).

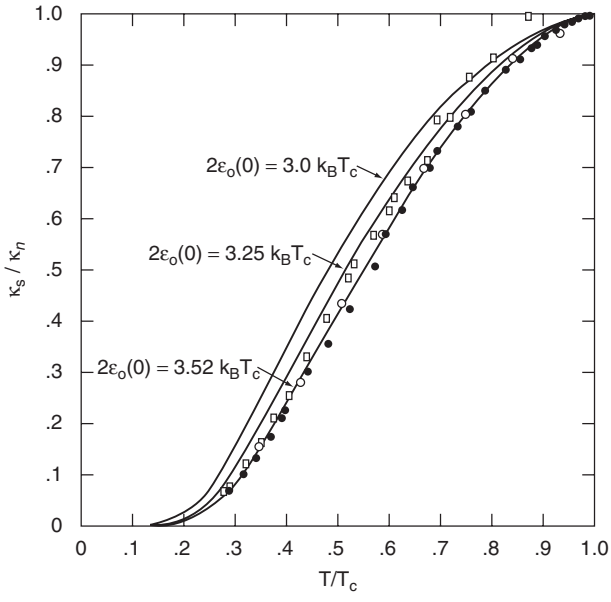

(a)

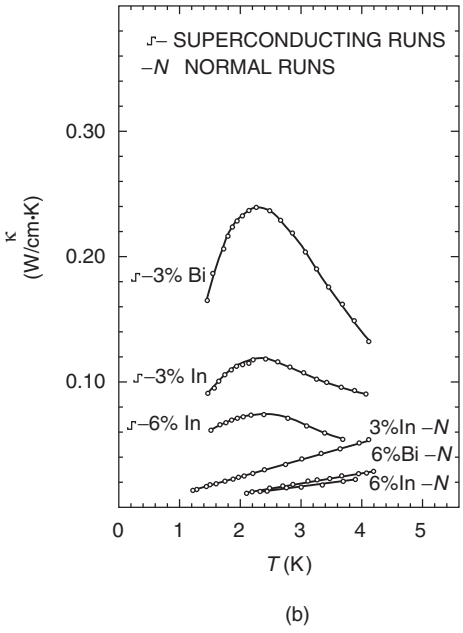

(b)

Figure W16.1. Thermal conductivity κ_s in the superconducting state and κ_n in the normal state. (*a*) The ratio κ_s/κ_n falls rapidly below unity for $T < T_c$ for the elemental superconductor Al. The solid curves represent the predictions of the BCS theory for various values of the superconducting energy gap in units of $k_B T_c$. (*b*) The quantity κ_s can be greater than κ_n below T_c, as illustrated for three superconducting alloys of Pb with In and Bi. [(*a*) From C. B. Satterthwaite, *Phys. Rev.*, **125**, 893 (1962). Copyright 1962 by the American Physical Society. (*b*) From P. Lindenfeld, *Phys. Rev. Lett.*, **6**, 613 (1961). Copyright 1961 by the American Physical Society.]

given as the sum of contributions from the superconducting and normal electrons by

$$G_s(T) = f_s(T)\left(-\frac{\mu_0 H_{c0}^2}{2}\right) + \sqrt{1 - f_s(T)}\left(-\frac{\gamma T^2}{2}\right). \tag{W16.1}$$

Here $-\mu_0 H_{c0}^2/2$ is the condensation energy per unit volume of the superconducting electrons relative to the normal state and $-\gamma T^2/2$ is the temperature-dependent part of the energy of the normal electrons. The parabolic dependence of the critical field $H_c(T)$ on T given in Eq. (16.6) can be shown to follow from this two-fluid expression for $G_s(T)$. It should be noted that while useful as a conceptual tool, the two-fluid model in this form cannot predict the observed exponential temperature dependence of the specific heat C_{es} as $T \to 0$ K.

W16.3 Superconducting Alloys of Metallic Elements

When alloys composed of superconducting elements such as Sn and In or Pb and Sn are prepared within the limits of their mutual solid solubility, the resulting single-phase superconductors also exhibit type I behavior as long as the electron mean free path l has not been decreased too much by the enhanced electron-impurity scattering present in the alloy. Further decreases in l result in an increase in the penetration depth λ and a decrease in the coherence length ξ until $\xi \approx l$ and $\kappa > 1/\sqrt{2}$. The alloy then becomes a type II superconductor.

The transition temperature T_c of such alloys typically decreases slowly, by 1 or 2%, when up to about 1 at % of alloying element is added, essentially independent of the host or the alloying element. It is believed that this is also a mean-free-path effect in which the decrease in l due to alloying eliminates the anisotropy of the energy gap present in the pure metal. Additional alloying beyond the level of ≈ 1 at % can lead to an increase or a decrease in T_c, depending on the nature of the host and alloying elements. When the alloying element possesses a magnetic moment (e.g., as for Fe or Mn), T_c is typically depressed to 0 K by only a few tens or hundreds of parts per million of the magnetic impurity.

Transition metal alloys are usually type II superconductors. In crystalline alloys of the $3d$, $4d$, and $5d$ transition metal elements such as the $4d$ alloys $Nb_{1-x}Zr_x$ and $Nb_{1-x}Mo_x$, it is observed that T_c has maxima for values of the average number z_{av} of valence electrons per atom near 4.7 and 6.5. This is at least partially an electron density-of-states effect since the electronic contribution to the alloy specific heat that is proportional to $\rho(E_F)$ also exhibits peaks for the same values of z_{av}. The BCS prediction of Eq. (16.27) indeed indicates that high T_c should be correlated with high $\rho(E_F)$, all other factors remaining constant. It is also interesting to note that lattice (i.e., structural) instabilities are observed in these alloys near the same electron concentrations where high T_c values are found. The BCC crystal structure is stable for $4.7 < z_{av} < 6.5$, while the HCP crystal structure is stable for both $z_{av} < 4.7$ and $z_{av} > 6.5$. From the BCS point of view it should not be surprising that electron density-of-states effects and lattice effects both influence T_c.

W16.4 Superconducting Intermetallic Compounds

Intermetallic compounds differ from metallic alloys in that they have well-defined compositions or limited ranges of composition. In addition, the elements present in a compound occupy specific, ordered sites in the unit cell instead of occupying random

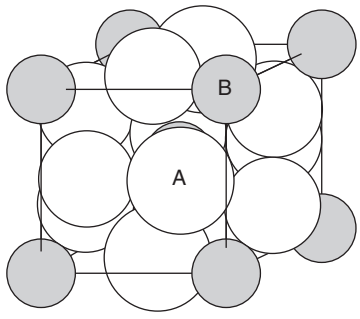

Figure W16.2. Cubic unit cell for the superconductors with the A15 crystal structure and the chemical formula A_3B. (From L. R. Testardi, *Rev. Mod. Phys.*, **47**, 637 (1975). Copyright 1975 by the American Physical Society.)

sites as in an alloy. For example, the two materials currently used in superconducting magnets, Nb_3Sn and $Nb_{0.36}Ti_{0.64}$, correspond to an intermetallic compound and a metallic alloy, respectively.

The A15 superconductors with the general formula A_3B (e.g., V_3Si, Nb_3Sn, Nb_3Ga, and Nb_3Ge) held the records for the highest T_c values from 1954 to 1986 when the discovery of the high-T_c cuprate superconductors occurred. The cubic crystal structure of these intermetallic compounds is shown in Fig. W16.2, where it can be seen that the B atoms occupy the sites of a BCC lattice. In this structure pairs of A atoms occupy adjacent sites in each of the six faces of the cubic unit cell, with three sets of nonintersecting linear chains of A atoms extending along the mutually perpendicular [100], [010], and [001] directions. Disorder in the chains due to deviations from the A_3B stoichiometry has been found to result in significant decreases in T_c.

Although there are at least 60 superconductors of the A_3B type, high T_c values are found only when the A atom is V, Nb, Mo, or Ta and the B atom is a metal such as Al, Ga, or Sn or a nonmetal such as Si or Ge. Thus the attainment of high T_c values is not strongly correlated with chemical bonding effects. Instead, the presence of a high density of states at the Fermi level associated with the exact A_3B stoichiometry is apparently necessary. The stoichiometric Nb-based compounds with B = Al, Ga, Si, and Ge are all metastable and are prepared by rapid quenching or other techniques. The highest T_c values are $T_c = 23.2$ K for Nb_3Ge and $T_c = 20.3$ K for Nb_3Ga. Specific heat and magnetic susceptibility studies have shown that Nb_3Ge and Nb_3Ga possess some of the highest values of $\rho(E_F)$ for the A15 superconductors. The normal-state properties of the A_3B compounds have also been studied widely to help understand the relatively high T_c values observed in these materials.

A list of some representative intermetallic compounds of different crystal structures, including several of the NaCl and A15 types, with T_c values near or greater than 10 K is presented in Table W16.1. This list serves to illustrate the extremely wide variety of materials and crystal structures in which superconductivity with $T_c \geq 10$ K is found. The superconducting AB compounds with the NaCl crystal structure form another important class of superconductors. The element A is typically a transition metal such as Nb, Mo, Ti, or Zr, while B is either C, N, O, or B. The highest T_c values are observed for those compounds with 9 or 10 valence electrons per formula unit (e.g., NbC or NbN and MoC, respectively).

TABLE W16.1 Transition Temperatures and Crystal Structures of Intermetallic Compound Superconductors

Superconductor	Structure Type[a]	T_c (K)
MoC	NaCl (FCC)	14.3
NbN_x[b]	NaCl (FCC)	17.3
PdH	NaCl (FCC)	9.5
PdD	NaCl (FCC)	11.6
HfV_2	$MgCu_2$, Laves (FCC)	9.4
$RhZr_2$	Al_2Cu (BCT)	11.3
V_3Si	UH_3, A15 (cubic)	17.1
Nb_3Sn	UH_3, A15 (cubic)	18.1
Nb_3Al	UH_3, A15 (cubic)	18
Nb_3Ga	UH_3, A15 (cubic)	20.3
Nb_3Ge	UH_3, A15 (cubic)	23.2
$LiTi_2O_4$	$MgAl_2O_4$, spinel (cubic)	13.7
YRh_4B_4	B_4CeCo_4 (tetragonal)	11.3
$LaMo_6Se_8$	$PbMo_6S_8$, Chevrel (trigonal)	11.4
YNi_2B_2C	— (tetragonal)	16.6

Source: Most data from D. R. Lide and H. P. R. Frederikse, eds., *CRC Handbook of Chemistry and Physics*, 75th ed., CRC Press, Boca Raton, Fla., 1994.

[a]The Bravais lattice is given in parentheses.

[b]The existence of nitrogen vacancies in NbN_x, with $x < 1$, allows T_c to be varied over a wide range. The T_c reported here is the highest known value for NbN_x.

The last entry, YNi_2B_2C, is a nonmagnetic member of the recently discovered family of rare earth nickel borocarbides (i.e., RNi_2B_2C, where R is a rare earth element). Superconducting members of this family include R = Y, Dy, Ho, Er, Tm, and Lu, of which Dy, Ho, Er, and Tm, and the R = Gd and Tb members undergo magnetic transitions to an antiferromagnetic state below a Néel temperature T_N. It is observed that $T_c > T_N$ for R = Ho, Er, Tm, and Lu, whereas the reverse is true for R = Dy. Study of these materials offers the opportunity of examining the interplay between magnetism and superconductivity.

W16.5 Further Discussion of Structure, Bonding, Composition, and Normal-State Properties of the Oxide-Based Ceramic Superconductors

The oxide $BaPb_{1-x}Bi_xO_3$ is superconducting for $0.05 < x < 0.3$ and can be considered to be the predecessor of the high-T_c cuprate superconductors discovered in 1986. For this mixed-valence material with a slightly distorted perovskite structure, the stoichiometric insulating $BaBiO_3$ compound with $x = 1$ can be represented by the formula $Ba^{2+}(Bi^{3+})_{0.5}(Bi^{5+})_{0.5}(O^{2-})_3$. When this oxide is doped with Pb^{4+} ions or when it is prepared in an oxygen-deficient form, the normally equal balance of closed-shell $Bi^{3+}(5d^{10}6s^2)$ and $Bi^{5+}(5d^{10})$ ions is disturbed and the concentration of electrons is modified. This material is semiconducting for $0.4 \leq x \leq 1$ and metallic for $x \leq 0.35$. By 1980, a T_c of 13 K had been achieved in this material for $x \approx 0.25$, corresponding to an electron concentration of about 3×10^{27} m^{-3}. This composition is actually closer to $BaPbO_3$, a metallic compound, than to the insulator $BaBiO_3$.

A related mixed-valence material that has the cubic perovskite structure for $x > 0.25$ is $Ba_{1-x}K_xBiO_{3-y}$, where $T_c \approx 30$ K has recently been achieved for $x \approx 0.4$. The charge carriers in this material have been shown to be electrons occupying a less than half-filled energy band. Although the K^+ ions donate one less electron to the structure than the Ba^{2+} ions they replace, the result of the doping is an electron-deficient metal rather than a metal in which the charge carriers are holes. The insulator $BaBiO_3$ can thus be transformed into a metallic superconductor either by doping with Pb on the Bi sites or with K on the Ba sites. The latter method is clearly more effective for obtaining higher T_c values.

Three of the superconductors shown in Fig. 16.17 are now described in more detail.

$La_{2-x}Sr_xCuO_4$ (LSCO). The stoichiometric compound La_2CuO_4 with nominal ionic charges La^{3+}, Cu^{2+}, and O^{2-} is an antiferromagnetic insulator with a Néel temperature $T_N = 340$ K. The Cu^{2+} ions have magnetic moments $m \approx 0.5\ \mu_B$. This compound becomes superconducting when doped with divalent ions such as Sr^{2+} or Ba^{2+} which replace some of the La^{3+} ions (e.g., $La_{2-x}Sr_xCuO_4$) or when doped with excess oxygen which enters the LaO layers as O^{2-} ions (e.g., La_2CuO_{4-y} with $y < 0$). Both types of doping result in the introduction of holes into the CuO_2 layers through the removal of electrons. In the first case, one of the electrons normally contributed by each La^{3+} ion to these layers is now no longer available. If an Sr^{2+} ion simply replaces a La^{3+} ion (similar to B^{3+} replacing Si^{4+} in crystalline Si) with no other changes taking place, hole doping will occur, an electron will be missing from some type of chemical "bond," and ionic charge neutrality will be violated. But if $Cu^{2+} \rightarrow Cu^{3+}$ in order to maintain ionic charge compensation, all the bonds will be satisfied and the hole will instead be present in the $3d$ shell of the Cu^{3+} ion. The related compound $Nd_{2-x}Ce_xCuO_4$ is an electron-type superconductor when doped with Ce^{4+} ions since each Ce^{4+} contributes an additional electron to the CuO_2 planes.

When doped at the level x greater than about 0.05, enough holes are introduced into the CuO_2 planes so that $La_{2-x}Sr_xCuO_4$ becomes a metal. It also becomes a superconductor whose highest $T_c \approx 40$ K is observed at the optimum doping level of $x \approx 0.16$. This is illustrated in the phase diagram for $La_{2-x}Sr_xCuO_4$ shown in Fig. 16.18. Notice the similarity of this phase diagram to that of $YBa_2Cu_3O_{7-x}$ given in the same figure. Regions where $La_{2-x}Sr_xCuO_4$ is an orthorhombic antiferromagnetic insulator and an orthorhombic or tetragonal metal are indicated.

As can be seen in Fig. 16.17, each CuO_2 layer in the La_2CuO_4 structure is separated from adjacent CuO_2 layers by pairs of LaO layers. This corresponds to a greater separation between CuO_2 planes than is found in $YBa_2Cu_3O_7$ and in the other cuprate superconductors where the CuO_2 planes are clustered in groups of two or three and are separated from each other only by single planes containing Y^{3+} or Ca^{2+} ions.

$YBa_2Cu_3O_{7-x}$ (YBCO). The orthorhombic unit cell of the $YBa_2Cu_3O_7$ structure is shown in Fig. W16.3 and the stacking sequence of the layers is shown in Fig. W16.4. It can be seen that the two CuO_2 layers in the unit cell are slightly puckered, while the CuO layer containing the linear $\ldots$CuOCuO$\ldots$ chains, taken to lie along the b axis, is planar. $YBa_2Cu_3O_7$ can be considered to be oxygen deficient in the sense that two oxygen atoms would appear to be missing from the hypothetical compound $YBa_2Cu_3O_9 = (YCuO_3)(BaCuO_3)_2$, which has the nominal perovskite stoichiometry. There are actually only eight possible oxygen sites in the unit cell, and one of these

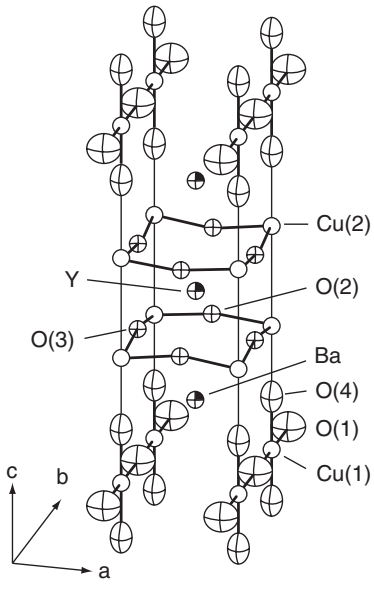

Figure W16.3. Orthorhombic unit cell of the $YBa_2Cu_3O_7$ structure. (From J. D. Jorgensen et al., *Phys. Rev. B*, **36**, 3608 (1987). Copyright 1987 by the American Physical Society.)

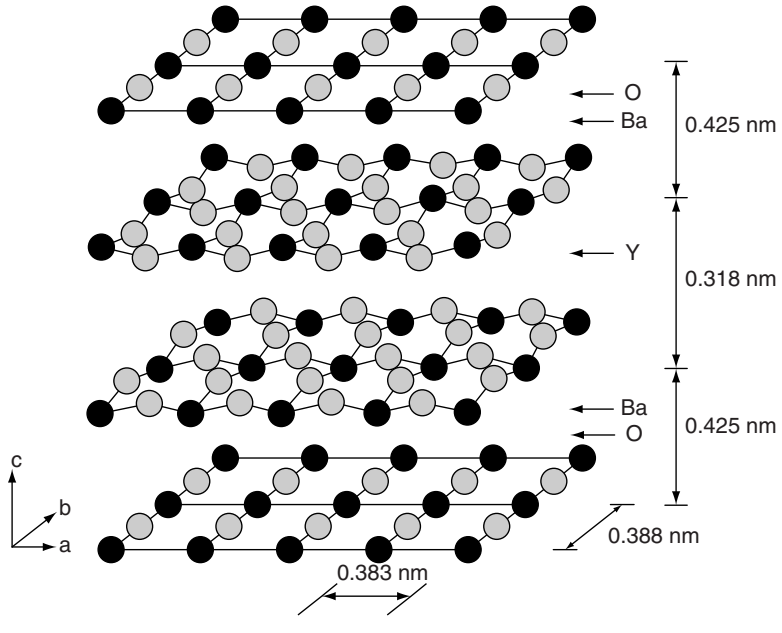

Figure W16.4. Stacking sequence of the layers parallel to the *c* axis in the $YBa_2Cu_3O_7$ structure. (From C. P. Poole, Jr., et al., *Copper Oxide Superconductors*, copyright 1988, John Wiley & Sons, Inc. Reprinted by permission of John Wiley & Sons, Inc.)

sites, in the layer with the CuO chains, is always vacant. Thus $YBa_2Cu_3O_7$ is, in fact, the correct chemical formula for this compound.

The $YBa_2Cu_3O_7$ structure differs from the other structures found in the high-T_c cuprate materials as follows:

1. In addition to the CuO_2 layers containing Cu ions with four NN O ions, there exist CuO layers consisting of CuO chains in which each Cu ion has two NN O ions in the layer and also two next-NN O ions just above and below it in the BaO layers at a distance of ≈ 0.18 nm. One half of the possible oxygen sites in this CuO layer are vacant, with the filled oxygen sites ordered along the *b* axis.
2. Overall ionic charge neutrality is maintained only if Cu^{3+} ions and/or oxygen vacancies are present in the structure. An alternative point of view is that ionic charge neutrality is in fact not required and that instead there are mobile holes in some of the copper–oxygen layers, as is discussed later.

The chemical bonding in $YBa_2Cu_3O_7$ is almost completely ionic for the Y^{3+} and Ba^{2+} ions but is of a mixed ionic–covalent type in the copper–oxygen layers. The interaction between the Y^{3+} and Ba^{2+} ions and the ions in the neighboring copper–oxygen layers is very weak. Thus the layers containing Y^{3+} and Ba^{2+} are insulating and the charge carriers are confined to the conducting copper–oxygen layers.

As mentioned earlier, if overall ionic charge neutrality were required within the $YBa_2Cu_3O_7$ formula unit with the assumed ionic charge states Y^{3+}, Ba^{2+}, and O^{2-}, the three Cu ions could have the following ionic charge states: Cu^{2+}, Cu^{2+}, and Cu^{3+} (i.e., one of the three Cu ions per formula unit would be trivalent). But requiring overall neutrality for ionic charge would mean that no delocalized charge carriers are present and $YBa_2Cu_3O_7$ would be an insulator. For $YBa_2Cu_3O_7$ to be a metallic conductor, the Fermi energy must lie within a partially filled energy band. This would result if all the Cu ions were actually in the Cu^{2+} charge state, resulting in one bonding electron per formula unit missing from the CuO_2 layers. This is equivalent to the point of view that there is one mobile hole per formula unit in the CuO_2 layers. In fact, it is not clear where the hole is present: on the Cu or O ions, in the CuO_2 layers, or in the CuO chains. If the Cu^{3+} ion is present instead, the hole would appear in the partially filled $3d$ shell of this ion.

There are at least two different ways to understand the presence of mobile holes in the stoichiometric $YBa_2Cu_3O_7$ compound in terms of chemical bonding arguments. According to a strictly ionic or *formal charge* viewpoint, if the charge states of the ions are assumed to be Y^{3+}, Ba^{2+}, Cu^{2+}, and O^{2-}, the net ionic charge per $YBa_2Cu_3O_7$ formula unit is $q_{\text{ion}} = +3e + 2(+2e) + 3(+2e) + 7(-2e) = +13e - 14e = -e$. Overall charge neutrality in the material could then be maintained by the presence of one hole with charge $+e$ per formula unit in the CuO_2 layers. From the alternative, covalent bonding point of view each of the four oxygen ions in the CuO_2 layers is assumed to have an ionic charge of $+2e$ (instead of $-2e$) and to contribute two electrons to the covalent bonds that it forms with its neighboring Cu^{2+} ions. According to this covalent point of view, each formula unit of $YBa_2Cu_3O_7$ has only 15 electrons available for bonding in the two CuO_2 layers, including three from the Y^{3+} ion, instead of the 16 required for the eight covalent bonds present. There is again one hole per formula unit present in the CuO_2 layers. Since the actual bonding

in the copper–oxygen layers is of a mixed ionic–covalent type, the true picture must lie somewhere between the ionic and covalent limits just described.

If oxygen vacancies are present in the material, as indicated by the formula $YBa_2Cu_3O_{7-x}$ with $x > 0$, then either fewer than one-third of the Cu ions would have to be in the +3 charge state in order to preserve ionic charge neutrality, or there would be fewer holes in the CuO_2 layers. If the oxygen vacancies occur in the CuO chains, corresponding to the formula $Y(BaO)_2(CuO_2)_2CuO_{1-x}$, the Cu^{2+} ions in the chains could donate electrons to the CuO_2 layers, thereby removing holes and causing a reduction in T_c.

The phase diagram for $YBa_2Cu_3O_{7-x}$ is shown in Fig. 16.18*b*. The physical properties of this material can be seen to be extremely sensitive to the oxygen stoichiometry, with structural and metal–insulator transitions along with rapid changes in both T_N and T_c occurring as x is varied. Note that $YBa_2Cu_3O_{7-x}$ becomes tetragonal and semiconducting for $x > 0.65$.

$HgBa_2Ca_2Cu_3O_8$ (HBCCO or Hg-1223). The current record for the highest known T_c, 135 K, is held by the $n = 2$ or Hg-1223 member of the $HgBa_2Ca_nCu_{n+1}O_{2n+4}$ family of compounds. For this family T_c increases with the number $(n + 1)$ of CuO_2 layers per unit cell (see Table 16.5). The unit cell of the $n = 1$ or Hg-1212 compound with $T_c = 128$ K is shown in Fig. W16.5. The excess oxygen that is apparently necessary for the superconductivity of $HgBa_2Ca_2Cu_3O_{8+x}$ resides in the Hg layers. The hole doping of the CuO_2 layers therefore originates from the Hg layer. Problems with control of composition have been found in this material due to loss of Hg during high-temperature processing.

Normal-State Properties. To obtain an understanding of the origins of the high-T_c superconductivity in the cuprates, it is first necessary to understand why they are

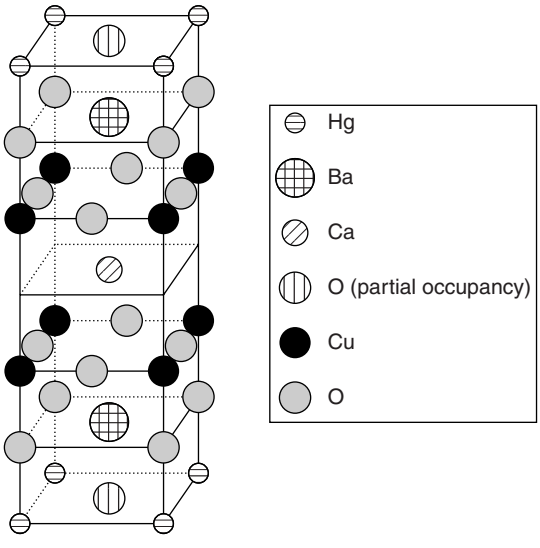

Figure W16.5. Tetragonal unit cell of the $n = 1$ or Hg-1212 member of the $HgBa_2Ca_nCu_{n+1}O_{2n+4}$ series of compounds with $T_c = 128$ K. (Reprinted from R.L. Meng et al., Physica **C214**, 307 (1993), copyright 1993, with permission from Elsevier Science.)

metallic conductors and not insulators in the normal state. Two viewpoints are possible: Chemical bonding effects lead to the existence of mobile charge carriers or the delocalization of the charge carriers can be understood as resulting from the particular electronic band structure of the material. Both points of view are useful and can provide important insights into the existence of the normal-state metallic behavior. Extrinsic effects such as doping can also play an important role in determining the conductivity of these materials in the normal state.

In the normal state above T_c, the cuprate materials are not typical metals and are not very good conductors of electricity. In addition, the electronic contribution to the specific heat in these materials is rather high, about a factor of 10 greater than that of simple metals such as Na or Cu. This latter result is attributed to the high effective masses of the carriers in high-T_c materials. The normal-state properties of these materials are strongly anisotropic, due to their tetragonal or orthorhombic crystal structures. Another unusual property of the high-T_c materials is that their electrical resistivities vary linearly with temperature above T_c.

From a covalent point of view, the chemical bonding between the Cu and O atoms in the copper–oxygen layers makes use of the s, p_x, p_y, and $d_{x^2-y^2}$ atomic orbitals of the $Cu^{2+}(3d^9)$ ions and the p_x and p_y atomic orbitals of the filled-shell O^{2-} $(2s^2 2p^6)$ ions, as shown in Fig. W16.6. These four atomic orbitals on Cu atoms hybridize to form square-planar dsp^2 hybrid orbitals which then overlap, that is, interact with the p_x and p_y atomic orbitals on adjacent O atoms (see Section W2.1 for a description of these atomic and hybrid orbitals). These interactions can then lead to the formation of σ-type molecular orbitals or chemical bonds which in the cuprate superconductors are actually of a mixed ionic–covalent nature due to the different electronegativities of the Cu and O atoms involved. It is clear that occupation of all four dsp^2 orbitals associated with the Cu^{2+} ion requires that two additional electrons be donated by other ions in the structure, such as Y^{3+} and Ca^{2+}. The electrons in these bonds form the valence energy bands of the material, which lie below the Fermi energy. From molecular orbital theory it appears that the states at E_F in $YBa_2Cu_3O_7$ will be antibonding orbitals of the Cu $d_{x^2-y^2}$ type. Most high-T_c cuprates display hole-type conduction in a conduction band that is nearly half full.

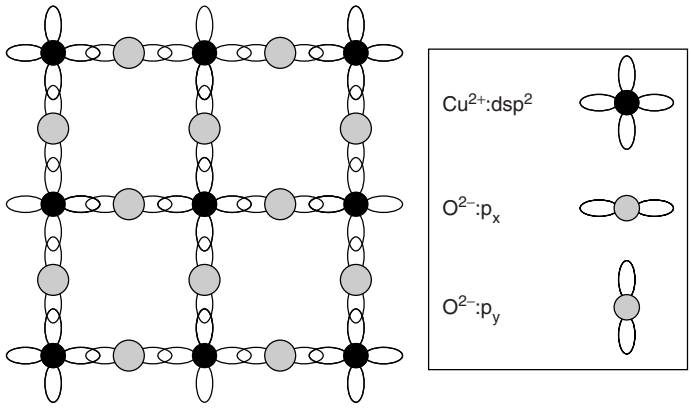

Figure W16.6. Chemical bonding between the Cu and O atoms in the copper–oxygen layers illustrated using the atomic orbitals involved: the square-planar dsp^2 hybrid orbitals of the Cu atoms and the p_x and p_y orbitals of the O atoms.

Rather than using the extended Bloch wavefunctions which are appropriate in good metals, the highly correlated nature of the electrons or holes in the copper–oxygen planes is often treated using tight-binding Hubbard models of the type used to describe the behavior of electrons associated with magnetic ions, as discussed in Chapter W9. The tight-binding approximation in two dimensions is applied to the Cu–O planes in Section 7.9. The goal of these models is to predict the occupancy by a pair of electrons of the orbitals on two adjacent sites. The effects of electrons hopping between the sites and of Coulomb repulsion between two electrons on a given site are the essential ingredients of these tight-binding models. It is possible that the important aspects of the high-T_c cuprate superconductivity can be understood in terms of the t–J version of the Hubbard model. Here t is the tunneling or hopping matrix element, J the exchange energy parameter given by $J = t^2/U$, and U the Coulomb repulsion energy for two electrons on the same site. In the limit $U \to 0$, the material will be a metal, while for $U \gg t$, the material will be an insulator with one electron localized on each site. The electrons in the high-T_c materials are *strongly correlated* because U is significantly greater than the average kinetic energy of the electrons at E_F. These strong correlations can induce both localized magnetic moments, which may undergo antiferromagnetic ordering and also localized electronic states leading to insulating behavior. An alternative approach to this problem is the *resonant valence bond* (RVB) model, in which the ground state corresponds to the usual chemical bonds in the copper–oxygen planes.

Calculations of the energy bands based on the three-state Hubbard model appropriate for the copper atom and two oxygen atoms per unit cell show that as a function of hole doping into the CuO_2 layers, peaks in the electronic density of states at E_F can lead to high T_c values. In addition, energy-band-structure calculations for these high-T_c materials have successfully predicted the observed anisotropy of the electrical conductivity and have provided useful information concerning the distribution of charge, thereby helping to clarify the chemical bonding present. Band-structure calculations predict that the electronic states in the vicinity of E_F are associated with the bonding orbitals in the copper–oxygen layers, which originate from the $Cu^{2+} d_{x^2-y^2}$ and the $O^{2-} p_x$ and p_y atomic orbitals.

Metal–insulator (MI) *transitions* can also appear within the framework of the Hubbard models as electrons are added to the energy bands. Metallic or conducting behavior will occur when E_F lies in a partially filled energy band. When E_F is nearer the top of an energy band and when there are unoccupied regions of the relevant Brillouin zone outside the Fermi surface, hole-type conduction can dominate the electrical behavior. MI transitions are indeed observed in the normal state of the high-T_c materials, such as $La_{2-x}Sr_xCuO_{4-y}$, as the composition changes. This material is an antiferromagnetic insulator with $T_N \approx 340$ K when undoped (i.e., for $x = 0$ and $y \geq 0$) and is metallic when doped (i.e., for $y = 0$ and $x > 0.05$; see Fig. 16.18).

All the high-T_c cuprate materials exhibit antiferromagnetic ordering in their insulating phases, which results from interactions between the Cu ($3d^9$) magnetic moments within the CuO_2 layers. The interaction responsible for the ordering is the indirect superexchange mechanism involving the copper $ds p^2$ hybrid orbitals and the oxygen p orbitals. The long-range order along the c axis is controlled by the much weaker interlayer coupling of the magnetic moments. The Néel temperature T_N decreases rapidly as doping increases and the metallic phase is approached. The incompatibility of the magnetic with the metallic phase occurs because the localized $3d$ electrons involved in the long-range magnetic order interact strongly with the delocalized charge carriers. As a result, the directions

of the magnetic moments of the localized $3d$ electrons fluctuate rapidly, destroying the antiferromagnetic long-range order. Short-range antiferromagnetic order can still exist below T_c, however. Phase diagrams showing the dependencies of structure and of T_c and T_N on the compositional parameter x are shown in Fig. 16.18 for $La_{2-x}Sr_xCuO_{4-y}$ and $YBa_2Cu_3O_{7-x}$. Note that $YBa_2Cu_3O_{7-x}$ is superconducting for x less than about 0.6 and is a semiconductor for $0.6 < x < 1$. The oxygen content determines both the hole concentration of this material and the shape of the Fermi surface. The Cu ions in YBCO apparently have local moments $m \approx 0.3\ \mu_B$ in the normal state above T_c.

Measurements of the Hall effect in the normal state of high-T_c materials have provided useful information on the signs and concentrations of the charge carriers, and, in conjunction with measurements of the electrical conductivity, have also helped to determine the charge carrier mobilities. These Hall effect studies have identified holes as the majority carriers in most high-T_c materials. The concentration of holes is observed to increase with increasing T and with doping (e.g., replacement of La^{3+} by Sr^{2+} in La_2CuO_4). In $La_{1.9}Sr_{0.1}CuO_4$ with $T_c \approx 35$ K, the hole concentration is $\approx 1 \times 10^{27}$ m^{-3}, at least a factor of 10 lower than that found in typical metals. This corresponds to about 0.1 hole per Cu atom, as expected from the Sr fraction. Hall effect studies in $YBa_2Cu_3O_{7-x}$ also identify holes as the charge carriers, with concentrations that decrease as x increases (i.e., as more O vacancies are present in the material).

The electrical resistivities of the high-T_c materials in their normal states are observed to have temperature dependencies of the form

$$\rho(T) = A + BT. \tag{W16.2}$$

This behavior is unusual since in conventional metals, $\rho(T) = A + BT^n$ with $n \approx 5$ as $T \to 0$ K. To illustrate this behavior, the measured resistivities for $YBa_2Cu_3O_7$ along the a, b, and c axes are presented in Fig. W16.7. The normal-state electrical

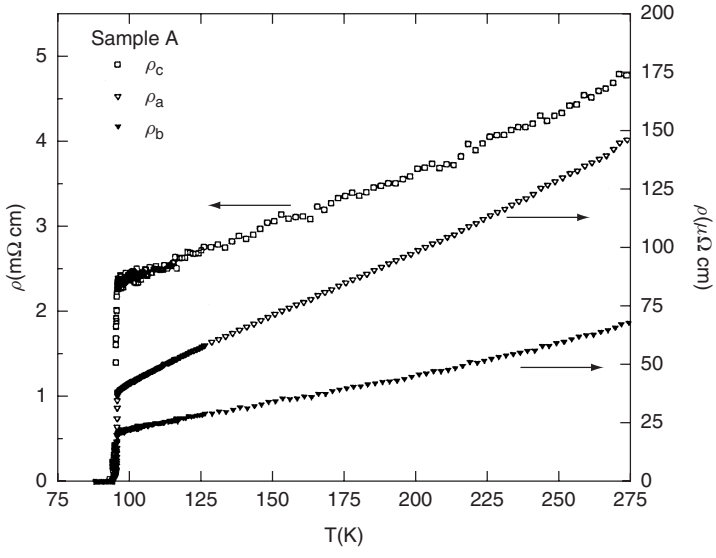

Figure W16.7. Measured electrical resistivities for $YBa_2Cu_3O_7$ along the a, b, and c axes. [From T. A. Friedmann et al., *Phys. Rev. B*, **42**, 6217 (1990). Copyright 1990 by the American Physical Society.]

resistivity of $YBa_2Cu_3O_7$ can be seen to be quite anisotropic, with the resistivity ρ_c perpendicular to the *ab* planes a factor of up to 150 times greater than the in-plane resistivities ρ_a and ρ_b. This behavior is consistent with the effective mass m_c^* for the motion of charge carriers along the *c* axis being much greater than m_a^* and m_b^* for motion in the *ab* plane. Evidence for localization of the charge carriers along the *c* axis has been found in some samples (i.e., ρ_c increases as T decreases). The lowest resistivity is found along the *b* axis, the axis of the Cu–O chains in the CuO planes, indicating that the Cu–O chains do contribute to the electrical conductivity in this material.

The temperature dependence of the resistivity of thin films of $DyBa_2Cu_3O_{7-x}$ as a function of x is shown in Fig. W16.8. The transition from semiconducting to metallic behavior can be observed as the concentration of oxygen vacancies decreases to zero. It should be noted that the replacement of Y by the rare earth atom Dy has essentially no effect on the superconducting or normal-state properties of this material.

Very similar values of the coefficient in Eq. (W16.2) of the linear term in $\rho_a(T)$ or $\rho_b(T)$ are found for most of the cuprate materials above their T_c values, indicating that the CuO_2 layers may exhibit a type of universal normal-state behavior in these materials.

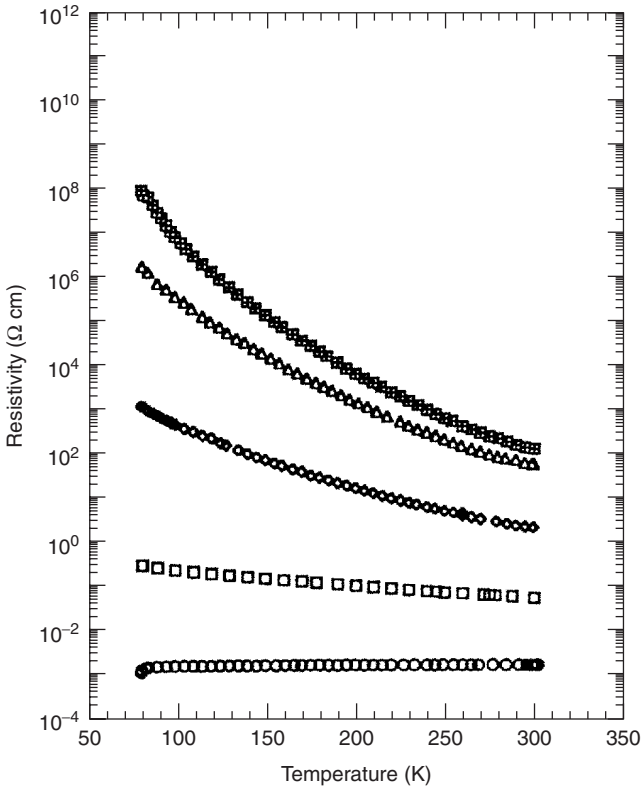

Figure W16.8. Temperature dependence of the resistivity of thin films of $DyBa_2Cu_3O_{7-x}$. The resistivity increases as x increases. The transition from semiconducting to metallic behavior occurs as the concentration of oxygen vacancies decreases. [From G. Yu et al., *Phys. Rev. B*, **45**, 4964 (1992). Copyright 1992 by the American Physical Society.]

W16.6 Further Discussion of Superconducting-State Properties of the Oxide-Based Ceramic Superconductors

An important property of the high-T_c cuprate superconductors is the strongly anisotropic nature of the superconductivity which results from the anisotropic tetragonal or orthorhombic structures of these materials. With the obvious exception of the transition temperature T_c, all the superconducting properties (i.e., critical fields and critical currents, superconducting energy gaps, penetration depths, coherence lengths, etc.) have values that are the same (or nearly the same) in the *ab* plane but which differ considerably from the corresponding values along the *c* axis. These anisotropies result from the anisotropic structure and effective masses m^* of the charge carriers in the normal state, with $m_c^*/m_a^* \approx 30$ in $YBa_2Cu_3O_7$. Even-higher effective-mass anisotropies are observed in the BSCCO and TBCCO families.

Since $\lambda \propto (m^*)^{1/2}$ [Eq. (16.10)] and $\xi \propto v_F \propto (m^*)^{-1/2}$ [Eq. (16.32)], the following inequalities can be expected to apply in high-T_c superconductors where $\xi \ll \lambda$ and $m_c^* \gg m_a^*$:

$$\lambda_c > \lambda_{ab} \gg \xi_{ab} > \xi_c, \tag{W16.3a}$$

$$\kappa_c \gg \kappa_{ab} \gg 1. \tag{W16.3b}$$

These predictions are consistent with the following results obtained for $YBa_2Cu_3O_7$:

$$\lambda_c \approx 500 \text{ nm} > \lambda_{ab} \approx 100 \text{ nm} \gg \xi_{ab} \approx 3 \text{ nm} > \xi_c \approx 0.5 \text{ nm} \tag{W16.4}$$

as well as the observed extreme type II behavior. The clean limit ordinarily applies to $YBa_2Cu_3O_7$ since the electron mean free path $l \approx 10$ nm is much greater than ξ_{ab} or ξ_c. As a result of this anisotropy, the cores of vortices will be circular when **H** is applied along the *c* axis and elliptical when **H** is applied parallel to the *ab* plane. In the mixed state with **H** applied along the *c* axis, the vortices are no longer continuous flux tubes but are proposed to be individual "pancake" vortices in a given CuO_2 layer which are only weakly coupled to each other through the intervening, nonsuperconducting layers. In addition, the low values of the coherence lengths ξ imply that the properties of these superconductors will be quite sensitive to deviations from chemical and structural uniformity.

Using the Ginzburg–Landau prediction that $H_{c2}(i) \propto \Phi_0/\xi_j\xi_k$, it can be shown that

$$\frac{H_{c2}(c)}{H_{c2}(ab)} = \sqrt{\frac{m_{ab}^*}{m_c^*}} \ll 1. \tag{W16.5}$$

Thus the upper critical field $H_{c2}(c)$ for H applied along the *c* axis in anisotropic superconductors such as $YBa_2Cu_3O_7$, where $m_c^* \gg m_a^*$ or m_b^* is predicted to be much less than the in-plane critical field $H_{c2}(ab)$. This is indeed observed to be the case for $YBa_2Cu_3O_7$, where it is found that $B_{c2}(c) = \mu_0 H_{c2}(c) \approx 20$ T, while $B_{c2}(ab) = \mu_0 H_{c2}(ab) \approx 70$ T at $T = 77$ K. The critical transport currents J_c in the high-T_c superconductors are also quite anisotropic, with the values of J_c parallel to the *ab* planes typically 10 times greater than J_c parallel to the *c* axis (see Table W16.2). Apparently, superconducting currents can flow along both the copper–oxygen layers and chains in $YBa_2Cu_3O_{7-x}$.

The superconducting energy gaps of the high-T_c superconductors are also observed to be quite anisotropic, with $2\varepsilon_{ab}(0) \approx$ (6 to 8) $k_B T_c$ and $2\varepsilon_c(0) \approx$ (2 to 4) $k_B T_c$. The energy gap in $YBa_2Cu_3O_7$ as measured by infrared reflectivity is quite anisotropic, with $2\varepsilon_{ab}(0) \approx 8k_B T_c$ and $2\varepsilon_c(0) \approx 3.5k_B T_c$, the latter being in good agreement with the weak-coupling BCS prediction and the former giving evidence for strong-coupling behavior. Electron tunneling studies tend to give a lower value for the $2\varepsilon_{ab}(0)$ gap, which is, however, still well above the BCS prediction of $3.52k_B T_c$.

The microwave surface resistance R_s of $YBa_2Cu_3O_{7-x}$ just below T_c shows evidence for an energy gap of magnitude $2\varepsilon(0) \approx 8k_B T_c$. Below $T_c/2$, however, the measured R_s is much higher than would be predicted by BCS on the basis of an energy gap of this size. These enhanced losses at lower T are due to unpaired charge carriers which are present due either to a much smaller energy gap or to the absence of a true gap (i.e., gapless superconductivity). It has been suggested that these may be carriers residing in the Cu–O chains. This "gapless" behavior is enhanced in oxygen-deficient samples with $x > 0$. An additional source of microwave losses in some samples could be weak links between the superconducting grains.

It is found in the high-T_c superconductors that ξ_c is comparable to the typical spacing between adjacent superconducting CuO_2 layers within a given unit cell and less than the distance between groups of CuO_2 layers in adjacent unit cells. Thus the CuO_2 layers are expected to be only weakly coupled to each other. The $HgBa_2Ca_1Cu_2O_6$ structure shown in Fig. W16.5, for example, has two CuO_2 layers within each unit cell which are separated from each other by Ca^{2+} layers and from the CuO_2 layers in adjacent unit cells by the BaO and Hg^{2+} layers.

The roles that the different layers or sites play in the high-T_c materials is illustrated by the effects that magnetic ions have on the superconductivity when they are introduced into the structure. Magnetic rare earth ions on the Y site in YBCO do not affect the superconductivity even if they order antiferromagnetically below T_c. The $3d$ magnetic ions on the Cu ion site destroy superconductivity, however, because they interact much more strongly with the superconducting electrons or holes.

While results of specific-heat studies show a jump at T_c, it has not been possible to check the BCS weak-coupling prediction that $C_{es}(T_c) - C_{en}(T_c) = 1.43\gamma T_c$, due to the inability to obtain reliable values for γ. Indeed, since H_{c2} is so large for these materials, it has not been possible to return to the normal state at sufficiently low T where the γT term could be extracted reliably from the measured specific heat. In the cuprates the phonon T^3 contribution to the specific heat dominates over the electron γT linear term at T_c. This behavior is opposite to that observed for relatively low-T_c superconductors such as Sn, Pb, and Nb.

W16.7 Unusual Superconductors

The wide variety of materials that become superconducting is further illustrated by several materials that may be considered to be unusual, not necessarily because the mechanism responsible for superconductivity is no longer the BCS indirect electron–phonon mechanism but because the existence or some aspect of the superconductivity is unexpected or unusual. Several examples are described next.

Intercalated Graphite. When K atoms are chemically inserted (i.e., *intercalated*) between the atomic planes of crystalline graphite, stoichiometric crystalline compounds

such as KC_8 can be obtained which are superconductors even though neither of the components (i.e., semimetallic graphite or metallic K) are themselves superconductors. The compound KC_8 retains the structure of graphite but with regular planar arrays of K atoms present which are separated along the c axis by single planes of C atoms. The superconductivity of KC_8 with $T_c \approx 0.39$ K apparently arises from the interactions between the electrons provided by the "donor" K atoms and the phonons of the planar graphite structure.

Doped Fullerites. In the solid state the C_{60} molecules known as *buckminsterfullerene*, as *fullerene*, or simply as *buckyballs* possess a three-dimensional FCC crystal structure known as *fullerite*. When the two tetrahedral and one octahedral vacant interstitial sites per C_{60} molecule in the FCC structure are occupied by alkali metal atoms such as K, the insulating C_{60} solid becomes a conductor and superconductivity is observed. These doped fullerites are known as *fullerides*. It has been observed that K_3C_{60} has $T_c = 19$ K, while a T_c value as high as 47 K has been found in Cs_3C_{60}. As in intercalated graphite (e.g., KC_8), the dopant alkali K^+ ions in solid K_3C_{60} provide the conduction electrons, while the C_{60} molecular structure provides both the necessary energy levels corresponding to extended or metallic electronic states and the phonons that are needed for the occurrence of superconductivity, assuming that the BCS indirect electron–phonon mechanism is operative.

Si and Ge Under Pressure. When Si and Ge are placed under pressures of about 120 atm, they undergo transformations to more highly coordinated metallic structures in which each atom has more than four NNs. In this metallic state they become superconducting at $T_c(\text{Si}) \approx 6.7$ K and $T_c(\text{Ge}) \approx 5.3$ K. Note that metallic Sn and Pb from the same column of the periodic table are conventional superconductors with $T_c = 3.7$ K and 7.2 K, respectively. Other normally nonmetallic elements which become superconducting due to phase transitions which occur under pressure include the group V elements P, As, Sb, and Bi and the group VI elements S, Se, and Te.

Heavy-Fermion Systems. There exist intermetallic compounds and metallic alloys in which the electronic contributions to the specific heat and to the Pauli paramagnetic susceptibility can be anomalously large, by about a factor of 100 above the predictions of the free-electron model. These anomalies can also occur for the rare earth elements, as described in Section 12.4, and are generally attributed to a strong, narrow peak in the density of electron states at E_F. Since $\rho(E_F)$ is proportional to the band-structure effective mass m^* of the electrons, these materials are usually called *heavy-fermion* or *heavy-electron systems*. When superconducting, these materials have relatively low T_c values: for example, $T_c = 0.43$ K for UPt_3, 0.6 K for $CeCu_2Si_2$, and 1.3 K for URu_2Si_2. In this sense these materials differ dramatically from essentially all other superconductors where a high electronic specific-heat coefficient γ is usually correlated with a high T_c value (see Fig. 16.19). These heavy-fermion systems often undergo antiferromagnetic ordering of the $4f$ or $5f$ magnetic moments at the Néel temperature T_N, which lies above the corresponding superconducting T_c.

A common component of these systems is an element with an unfilled f shell (e.g., the rare earth Ce or the actinide U with $4f^2$ and $5f^3$ electron configurations, respectively). These $4f$ or $5f$ electrons apparently hybridize or mix strongly with the conduction electrons, resulting in a narrow energy band that overlaps the Fermi

energy of the material. The mechanism for superconductivity in these heavy-fermion systems has not yet been identified. It is possible that the indirect electron–phonon BCS mechanism does not apply.

Charge-Transfer Organic Solids. Some unusual charge-transfer compounds composed of organic molecular *electron-donor* ions such as BEDT-TTF$^+$ (ET for short; $[C_2S_2C_2S_2(CH_3)_2]_2^+$) and inorganic *electron-acceptor* ions such as $Cu(NCS)_2^-$ are highly conducting materials that can become superconducting at temperatures as high as $T_c = 10$ K. The properties of these charge-transfer organic superconductors are usually highly anisotropic. They exhibit nearly one- or two-dimensional conducting behavior, due to the presence in the structures of stacked planar aromatic rings connected by π bonds. In this sense there are some interesting similarities between these materials and the high-T_c cuprate superconductors.

W16.8 Further Discussion of Critical Currents

The critical transport current density J_c in the mixed state of a type II superconductor will be the current for which the Lorentz forces exceed the average *pinning* forces that tend to prevent vortex motion. Thermal *depinning* of vortices can also lead to vortex motion and hence losses. This will be especially important in the high-T_c materials where the available thermal energy k_BT can exceed the depth of the typical pinning potential well. The introduction of defects such as dislocations in a cold-worked material can lead to significant increases in the critical current without at the same time affecting the upper critical field H_{c2}. The introduction of defects corresponding to a certain size, type, and concentration of pinning center can be carried out through a variety of techniques, including irradiation with protons or neutrons. The development of superconducting materials with sufficiently strong pinning forces to allow the attainment of high current densities in the presence of high magnetic fields is an area of great current interest.

Some typical values of critical transport current densities J_c for superconductors of technological importance are given in Table W16.2. Also specified are the temperature and applied magnetic field at which J_c was measured. In the case of an applied field, the direction of current flow is perpendicular to the direction of **H**.

It can be seen from Table W16.2 that the highest critical currents in $YBa_2Cu_3O_7$ are found in thin films rather than in single crystals. Apparently, the films contain more pinning centers than do the single crystals. For the single crystals, J_c can be increased by a factor of about 100 through neutron or proton irradiation. Oxygen vacancies in $YBa_2Cu_3O_{7-x}$ may be the most important pinning centers. Grain boundaries between neighboring $YBa_2Cu_3O_7$ crystallites which are at low angles with respect to the CuO_2 planes are necessary for the achievement of high critical current densities since high-angle grain boundaries can act as weak links between the grains. It can also be seen that for a given superconductor, J_c decreases with increasing T and also with increasing applied external H. This temperature dependence for J_c is consistent with the prediction of the G-L theory that

$$J_c(T) = H_c(T)/\lambda(T). \tag{W16.6}$$

This critical current density is essentially equal to the depairing current density determined by equating the kinetic energy density of the current-carrying electrons to the

TABLE W16.2 Critical Current Densities J_c for Superconductors of Technological Importance

Superconductor	T (K)	J_c (MA/cm^2)	$B = \mu_0 H$ (T)	Comments
$Nb_{0.36}Ti_{0.64}$	4.2	0.37	5	Filament
Nb_3Sn	4.2	>0.1	12	Filament
$YBa_2Cu_3O_{7-x}$	5	1.4	0–1	Single crystal, $B \perp ab$ plane
	77	0.01	0.1	Single crystal, $B \perp ab$ plane
	77	0.0043	1	Single crystal, $B \perp ab$ plane
	4.2	60	0	Epitaxial film
	4.2	40	8	Epitaxial film, B in ab plane
	4.2	6	8	Epitaxial film, $B \perp ab$ plane
	4	1300	0	Epitaxial film, 500 nm thick
	77	1	0	1 to 2-μm films on metal tapes
	77	0.1	5	1 to 2-μm films on metal tapes
$Bi_2Sr_2CaCu_2O_8$	4.2	0.17	30	Filaments in Ag-sheathed tape
$Bi_{2-x}Pb_xSr_2Ca_2Cu_3O_{10}$	4.2	0.1	25	Filaments in Ag-sheathed tape
	77	0.05	0	Filaments in Ag-sheathed tape

Source: Data collected from various sources, including C. P. Poole, Jr., H. A. Farach, and R. J. Creswick, *Superconductivity*, Academic Press, San Diego, Calif., 1995, p. 392.

superconducting condensation energy. The depairing current density corresponds to the excitation of charge carriers across the superconducting energy gap due to their increased kinetic energy associated with the flow of transport current. Measured values of J_c often fall well below this prediction, due to the vortex motion, which is not accounted for in the G-L theory.

A vortex that is pinned and therefore unable to move also hinders the motion of neighboring vortices. Thus vortex motion and pinning are collective processes, especially for fields near H_{c2}. When the pinning forces are not strong enough to prevent vortex motion, the superconductor is termed "*soft*", while the reverse is true in "*hard*" superconductors. Hard superconductors exhibit magnetization curves which show strong hysteresis effects due to the trapping of flux caused by vortex pinning. Examples of hysteretic magnetization curves for the type II high-T_c superconductor $YBa_2Cu_3O_7$ are shown in Fig. W16.9. As the superconductor is cycled around the magnetization loop the energy dissipated in the material per unit volume is proportional to the area inside the hysteresis loop [see Eq. (17.10)]. The remanent magnetization M_r and the coercive field H_c are defined as shown. The magnetization M_r remaining

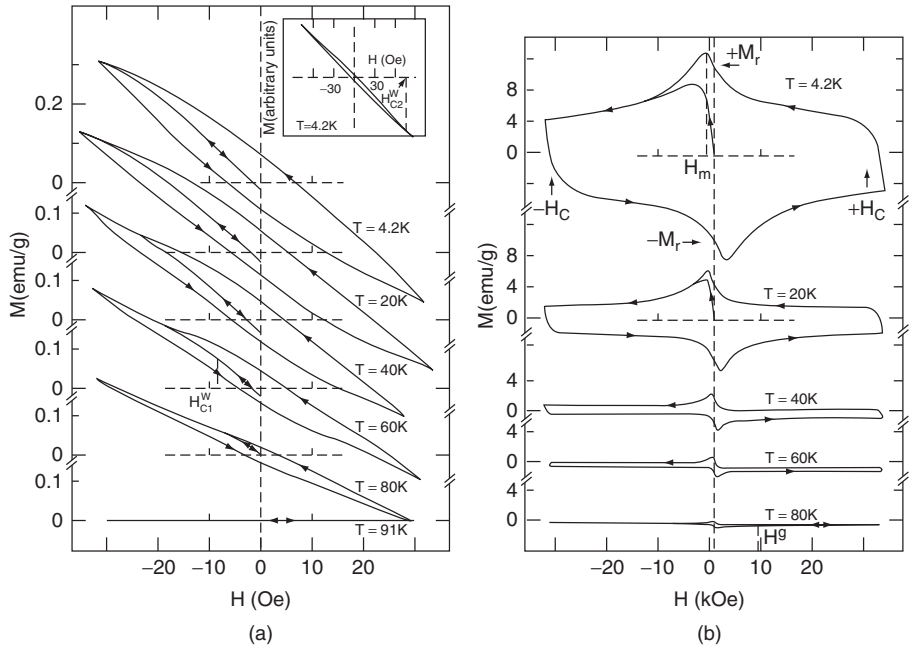

Figure W16.9. Magnetization curves for the high-T_c superconductor $YBa_2Cu_3O_7$: (*a*) low-field loops; (*b*) high-field loops. The observed hysteresis is due to the trapping of flux caused by the pinning of vortices. The remanent magnetization M_r and the coercive field H_c are defined as shown. The quantities H_m and H^g are the magnetic fields at which M reaches a maximum and above which M is reversible, respectively. (From S. Senoussi et al., *J. Appl. Phys.*, **63**, 4176 (1988). Copyright 1988 by the American Institute of Physics.)

at $H = 0$ corresponds to the magnetic moment per unit volume of the shielding supercurrents which flow around regions of *trapped flux*. These regions of trapped flux are either void regions or regions that remain normal even after most of the material has returned to the superconducting state. The fraction of the sample that remains in the normal state at $H = 0$ is proportional to M_r.

The phenomenon of *flux creep* can occur in the presence of a transport current flowing through a superconductor when the pinning forces are strong, while the process of *flux flow* occurs when the pinning forces are weak. In both cases, dissipation is present. The results of measurements of the critical currents in two $Nb_{0.5}Ta_{0.5}$ alloys with different defect concentrations are shown in Fig. W16.10. The voltage–current curves shown have intercepts on the current axis equal to i_c, the critical current at which a voltage first appears in the superconductor. The slopes dV/di for $i > i_c$ yield the *flux-flow resistance* R_{ff}, which corresponds to a resistivity $\rho_{\text{ff}} \approx \rho_n(B/B_{c2})$, where ρ_n is the normal-state resistivity and B is the average flux density in the mixed state. Note that i_c is higher for the alloy with the higher defect or pinning center concentration, while the flux-flow resistances are independent of the defect level. The resistance R_{ff} increases with increasing magnetic field, as the vortices move faster through the material, and approaches the normal-state resistance as $H \to H_{c2}$.

The collective motion of vortices can be understood in terms of the flow of a two-dimensional viscous fluid. When the vortices are strongly pinned, the vortex fluid

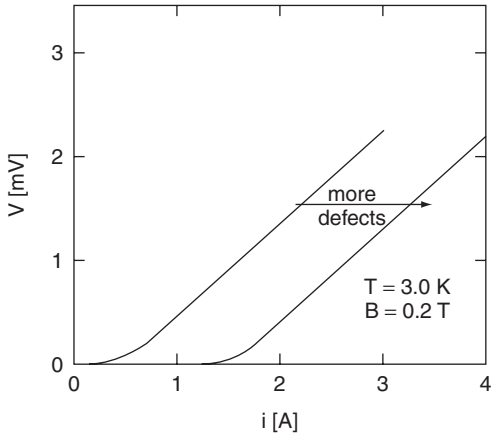

Figure W16.10. Results of measurements of the critical currents in two $Nb_{0.5}Ta_{0.5}$ alloys with different defect concentrations. [From A. R. Strnad, C. F. Hempstead, and Y. B. Kim, *Phys. Rev. Lett.*, **13**, 794 (1964). Copyright 1964 by the American Physical Society.]

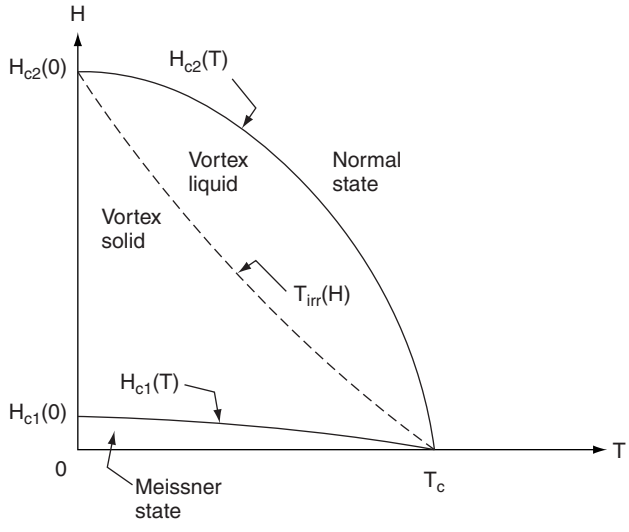

Figure W16.11. Magnetic phase diagram for a type II high-T_c superconductor. The vortex solid (or glass) and vortex liquid phases in the mixed state between H_{c1} and H_{c2} are shown.

instead forms a solid phase. When long-range order is present in the solid phase, a *vortex lattice* is formed (see Fig. 16.11). The vortex solid is termed a *vortex glass* if only short-range order is present, due to the spatial randomness of the pinning centers. A schematic magnetic phase diagram for a type II high-T_c superconductor showing the vortex solid and liquid phases in the mixed state between H_{c1} and H_{c2} is presented in Fig. W16.11 for H perpendicular to the *ab* planes. In practice, H_{c1} can be orders of magnitude less than H_{c2}. This phase diagram is considerably more complicated than the simpler version given in the textbook in Fig. 16.7*c* for low-T_c conventional type II superconductors. The fact that dissipation-free transport of current

can occur only in the vortex solid phase where the vortices are strongly pinned has complicated the development of the high-T_c superconductors for high-field current-carrying applications. Recent progress that has been made in this area is discussed later when large-scale applications of superconductivity are described.

Note that the vortex solid "melts" as either higher temperatures (thermal activation) or higher magnetic fields are applied to the superconductor. Under these conditions the vortices become depinned from defects and decoupled from each other. This transition occurs at the *irreversibility temperature* T_{irr} shown in Fig. W16.11, which defines the melting line separating the vortex solid and liquid phases. This boundary also serves to define the temperature-dependent *irreversibility magnetic field* H_{irr}. Magnetic flux-dependent reversibility is observed in the vortex liquid phase, while magnetic irreversibility is found in the vortex solid phase. Flux trapping therefore occurs much more readily in the vortex solid phase. Even before the flux lattice melts, flux creep can still occur for $T < T_{\text{irr}}$ due to thermal activation of the vortices out of their pinning potential wells. The velocity of the resulting flux motion is given by

$$v = v_{\text{o}} \exp\left(-\frac{U}{k_B T}\right), \tag{W16.7}$$

where the activation energy U is a complicated function of current density J, magnetic field H, and temperature T. Note that $U \to 0$ as $J \to J_c$. The energy U can have values ranging from tenths of an electron volt up to several electron volts. The vortex liquid phase is more evident and occupies a greater portion of the phase diagram for high-T_c superconductors than for conventional superconductors, due to the higher T_c values of the former, which enhance the effects of thermal depinning. The boundary between the vortex solid and liquid phases can be shifted to higher magnetic fields and temperatures by introducing additional pinning centers into the superconductor which help to stabilize the vortex solid phase.

Although defects are useful for the pinning of vortices, if too much of the superconductor is defective (e.g., nonsuperconducting), the necessary superconducting current paths will not be present.

W16.9 Further Discussion of Large-Scale Applications

Since Nb_3Sn is inherently brittle and cannot be drawn down by itself into wires, the wire used for superconducting applications is typically formed by inserting Nb rods into Sn tubes which are then drawn down repeatedly to a certain size. The thin rod thus formed is then inserted into a Cu tube and drawn down repeatedly again. Heat treatment is then used to form the Nb_3Sn superconducting compound at the Nb/Sn interfaces. The resulting wire can carry high currents in a lossless manner and is also relatively flexible and mechanically stable due to the copper sheathing. Nb–Ti alloys do not require such complex processing since they have the advantage of being inherently ductile.

The *pinning centers* in Nb–Ti alloys can be created by annealing processes that cause the precipitation of clusters of metallic α-Ti with $T_c \approx 0.4$ K. After drawing the wire down, the Ti pins typically are $\approx$ 1 to 2 nm in size and spaced $\approx$ 3 to 6 nm apart. Pinning centers can also be introduced into the Nb–Ti alloy in an artificial manner by placing a macroscopic pin material such as a low-field superconductor (Nb

or Ti), a normal metal (Cu), or even a ferromagnetic metal (Ni or Fe) into the alloy before drawing it down. The ferromagnetic pins are especially effective because of the destructive effect that magnetic moments have on superconductivity.

The high-T_c cuprate superconductors are ceramics and hence are inherently brittle. This property presents a serious challenge for the fabrication of long wires of these materials. The current-carrying capacity of polycrystalline high-T_c samples can be improved by techniques which enhance intergrain contact so that superconducting currents can easily flow from one grain to another, preferably parallel to the *ab* planes, which have higher critical currents. High-angle grain boundaries in high-T_c materials which form weak links between adjacent superconducting crystalline grains will limit the lossless flow of supercurrents through the materials.

High-T_c superconductors tend to have weaker pinning forces than elemental or intermetallic compound superconductors, due in part to the fact that they have "pancake" vortices (i.e., the supercurrents surrounding each vortex exist only within the CuO_2 layers). Therefore, the vortices in adjacent CuO_2 layers are not as strongly coupled to each other as in superconductors whose structures are three-dimensional. Intrinsic pinning in high-T_c materials refers to the difficulty that vortices have in moving perpendicular to the copper–oxygen layers through the isolation barriers composed of layers of atoms which are essentially normal material. The pancake vortices can move within the *ab* planes, and defects confined to a given layer will affect only the motions of vortices in that layer. Flux creep occurs much more rapidly when vortices move parallel to the copper–oxygen layers than when the vortex motion is perpendicular to the layers.

The vortex solid is much more stable in $YBa_2Cu_3O_7$ than in other high-T_c superconductors, such as the BSCCO family. This is likely the result of pinning centers with deeper potential wells in $YBa_2Cu_3O_7$. Also, because the spacing between groups of superconducting CuO_2 layers is smaller in $YBa_2Cu_3O_7$ than in the BSCCO family, the pancake vortices are more strongly coupled along the c axis in $YBa_2Cu_3O_7$. Nevertheless, $YBa_2Cu_3O_7$ tends to have lower critical currents due to weak links between adjacent superconducting grains and is more difficult to prepare in wire form.

A method similar to that used for Nb_3Sn is employed for some high-T_c materials where a silver tube is filled with powder of, for example, Pb-stabilized $Bi_{2-x}Pb_xSr_2Ca_2Cu_3O_{10}$. The filled tube is then drawn, rolled, and sintered, resulting in a material that is fairly well aligned with the superconducting CuO_2 layers of the crystallites lying roughly parallel to each other. This desirable platelike microstructure of the BSCCO superconductors results from the ease of cleavage of the two adjacent BiO layers perpendicular to the c axis (see Fig. 16.17). The success of this processing method is due to the chemical stability of the high-T_c materials in the presence of Ag and also to the ease of diffusion of oxygen through the Ag sheath, that allows the proper stoichiometry to be achieved following sintering or annealing in O_2. Heavy-ion irradiation of $Bi_2Sr_2Ca_2Cu_3O_{10+x}$/Ag tapes introduces columnar defects in the form of amorphous regions ≈ 7.4 nm in diameter surrounded by an associated strain field. These columnar defects are currently the most efficient pinning centers known for flux lines in layered superconductors, such as the high-T_c cuprates.

Although some important fabrication problems have been solved, the losses in $Bi_2Sr_2Ca_2Cu_3O_{10}$ wires remain too high for their application at $T = 77$ K in high magnetic fields. When used in applications such as superconducting magnets or electrical machinery where high magnetic fields are present, this material must be kept below $T = 25$ to 30 K in order to operate in the vortex solid region of the magnetic

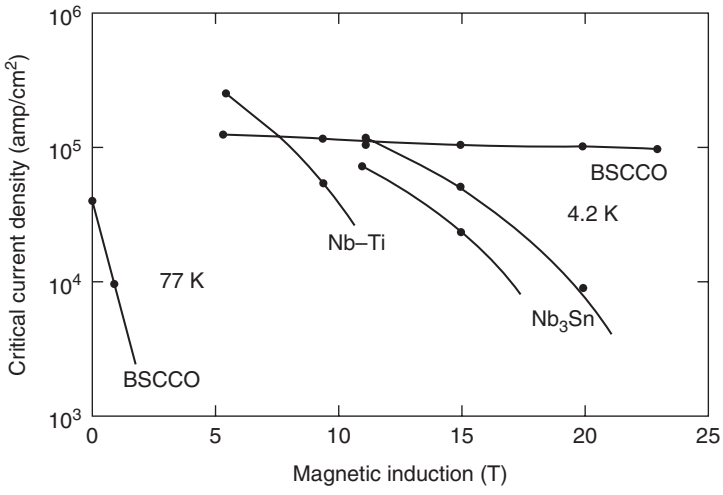

Figure W16.12. Magnetic field dependence of the critical current density in BSCCO tapes sheathed in Ag compared with J_c for Nb–Ti and Nb_3Sn. (From D. Larbalestier, *Phys. Today*, **44**, 74 (1991). Copyright 1991 by the American Institute of Physics.)

phase diagram, where resistive losses are low. The magnetic field dependence of the critical current density in BSCCO tapes sheathed in Ag is presented in Fig. W16.12 and compared with J_c for commercial Nb–Ti and Nb_3Sn superconductors. It can be seen that $Ba_2Sr_2Ca_2Cu_3O_{10}$ retains its ability to carry transport currents to much higher fields at $T = 4.2$ K, but not at 77 K, than the Nb-based superconductors.

The growth of $YBa_2Cu_3O_7$ on flexible Ni alloy tapes with matching thermal expansion coefficients and the use of an intermediate buffer layer of yttria-stabilized zirconia to prevent chemical interactions has proven to be a useful method of synthesizing superconducting wire which can operate at $T = 77$ K with $J_c \approx 1$ MA/cm^2 in zero magnetic field (see Table W16.2). When operated at $T \approx 64$ K, short lengths of these $YBa_2Cu_3O_7$ conductors have critical current densities in fields up to 8 T, which are equal to those of the currently used Nb–Ti and Nb_3Sn materials at $T = 4.2$ K.

In a high-T_c superconductor such as $YBa_2Cu_3O_7$, where $\xi \approx 1$ to 2 nm, the optimum configuration of pinning defects corresponds to a very high density of small defects. Thus any form of atomic disorder should serve as a pinning center in these high-T_c superconductors. The difficulty is in introducing this atomic-level disorder in a reproducible manner.

W16.10 Josephson Effects

When both sides of a tunnel junction are superconducting (e.g., for an S–I–S junction), an additional contribution to the usual quasiparticle or normal-electron tunneling current can arise from the passage of a supercurrent of Cooper pairs across the junction even when the applied voltage $V = 0$. The resulting *Josephson current* has been observed experimentally, and the related *Josephson effects* serve as the basis for the operation of SQUIDs as the most sensitive existing sensors of magnetic flux. The Josephson relations that are the basis of the Josephson effects are derived next.

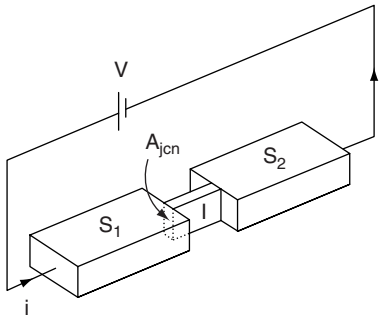

Figure W16.13. Two superconductors, S_1 and S_2, which are part of an S_1–I–S_2 Josephson tunnel junction are weakly coupled to each other through an insulating barrier or weak link I.

Consider two superconductors S_1 and S_2 which are part of an S_1–I–S_2 *tunnel junction* (Fig. W16.13). S_1 and S_2 are weakly coupled to each other through an insulating barrier I, which serves as a weak link. The time-dependent Schrödinger equations for the macroscopic superconducting wavefunctions Ψ_1 and Ψ_2 in the two superconductors are given by

$$\begin{aligned} i\hbar\frac{d\Psi_1}{dt} &= eV\Psi_1 + K\Psi_2, \\ i\hbar\frac{d\Psi_2}{dt} &= eV\Psi_2 + K\Psi_1. \end{aligned} \tag{W16.8}$$

Here the strength of the coupling through the barrier is represented by the parameter K. The physical significance of these equations is that the wavefunctions and the corresponding Cooper pairs of the two superconductors can overlap each other within the junction region. When the overlap is sufficiently strong, the phases of the two wavefunctions will be coupled to each other and Cooper pairs will be able to tunnel across the junction even for $V = 0$. Note that these equations are also appropriate for the case when a voltage is applied across the junction.

The wavefunctions Ψ_1 and Ψ_2 can be written as the products of an amplitude factor expressed in terms of the concentration n_s of superconducting electrons and a phase factor as follows:

$$\begin{aligned} \Psi_1(t) &= \sqrt{n_{s1}(t)}e^{i\theta_1(t)}, \\ \Psi_2(t) &= \sqrt{n_{s2}(t)}e^{i\theta_2(t)}, \end{aligned} \tag{W16.9}$$

where $\theta(t) = \theta_2(t) - \theta_1(t)$ is the phase difference between the wavefunctions on opposite sides of the junction. Note that $|\Psi_1|^2 = n_{s1}$ and $|\Psi_2|^2 = n_{s2}$. When these expressions for Ψ_1 and Ψ_2 are substituted into Eq. (W16.8), the following results can be derived:

$$\hbar\frac{dn_{s1}}{dt} = 2K\sqrt{n_{s1}n_{s2}}\sin\theta, \tag{W16.10a}$$

$$\hbar\frac{dn_{s2}}{dt} = -2K\sqrt{n_{s1}n_{s2}}\sin\theta, \tag{W16.10b}$$

$$\frac{d\theta}{dt} = \frac{2eV}{\hbar}. \tag{W16.11}$$

The *Josephson current* $i(t)$ that can flow through the junction is given in terms of the rates of change with time of n_{s1} and n_{s2} by

$$i(t) = e\left(V_1 \frac{dn_{s1}}{dt} - V_2 \frac{dn_{s2}}{dt}\right). \tag{W16.12}$$

Here the volumes V_1 and V_2 correspond to the regions in the superconductors in which the changes in n_{s1} and n_{s2} occur, typically within a coherence length ξ of the junction. The substitution of Eqs. (W16.10*a*) and (W16.10*b*) into Eq. (W16.12) results in the following current-phase relationship:

$$J(t) = J_c \sin\theta(t). \tag{W16.13}$$

The Josephson current density is defined as $J = i/A$, where A is the cross-sectional area of the junction. Thus it is evident that an applied current will control the phase difference θ across the junction. The prefactor J_c, the *critical current density*, corresponds to the maximum current that can flow through the junction when $V = 0$. It is given by

$$J_c = \frac{4eK\sqrt{n_{s1}n_{s2}}}{\hbar} \frac{(V_1 + V_2)}{A}. \tag{W16.14}$$

Equations (W16.11) and (W16.13) are known as the *Josephson relations* and are the fundamental expressions describing the tunneling of Cooper pairs.

Four distinct types of phenomena involving the tunneling of Cooper pairs across a *Josephson junction* are discussed next.

DC Josephson Effect. The *dc Josephson effect* corresponds to the spontaneous flow of the direct tunneling current $J = J_c \sin\theta_0$ given in Eq. (W16.13) for $V = 0$. Since in this case $d\theta/dt = 0$ from Eq. (W16.11), the difference in phase θ_0 of the superconducting order parameter across the junction will be constant. Thus a superconducting Josephson junction can act as a direct-current source. It can be seen from Eq. (W16.14) that $J \propto n_s(T)$. It follows, therefore, that $J_c(T)$ will increase from 0 at $T = T_c$ and will reach a finite value at $T = 0$ K, which can be shown to be about 80% of the corresponding normal-metal tunneling conductance. For the current to exceed J_c, a voltage must be present across the junction.

There exist junctions or weak links between pairs of superconductors in which the current does not exhibit the sinusoidal dependence on the phase difference θ expressed in Eq. (W16.13). Although these are not Josephson junctions, they are nevertheless sensitive to θ and to changes in the magnetic flux Φ through the junction. True Josephson tunneling can be observed only for the case of very thin barriers, ≈ 1 nm thick.

AC Josephson Effect. When a constant voltage is applied across the Josephson junction, it follows from Eq. (W16.11) that the phase difference θ will change linearly with time according to

$$\theta(t) = \frac{2eVt}{\hbar} + \theta_0. \tag{W16.15}$$

In additional to the usual tunneling of normal electrons or quasiparticles, there will also be a sinusoidal or alternating tunneling current of Cooper pairs in this case given by

$$J(V,t) = J_c \sin\left(\frac{2eVt}{\hbar} + \theta_0\right). \tag{W16.16}$$

This alternating current flows through the junction at the Josephson angular frequency $\omega_J = 2eV/\hbar = 2\pi V/\Phi_0$, where Φ_0 is the flux quantum. This current corresponds to the *ac Josephson effect*. For an applied voltage $V = 1$ mV, the corresponding *Josephson frequency* $f_J = \omega_J/2\pi = 4.84 \times 10^{11}$ Hz is in the RF region. The junction can therefore act as a source of RF radiation whose frequency, 4.84×10^{11} Hz/mV, can be controlled precisely through the applied voltage. An interesting application of the ac Josephson effect is in an extremely precise determination of the ratio e/h, which is used in establishing a self-consistent set of recommended values of the fundamental physical constants. The amplitude J_c is also a function of the applied voltage and reaches a maximum at $eV = 2\varepsilon$, the superconducting energy gap. Note that in this case a photon is involved in the Cooper pair tunneling for conservation of energy because, with $|V| > 0$, the condensed states are no longer aligned across the junction.

A detailed analysis of the response of a Josephson junction when "driven" by a constant voltage must also take into account the capacitance of the junction and also any nonzero normal conductance that the barrier may have if it is not a perfect insulator. While the response of the junction approaches normal-metal tunneling for $eV > 2\varepsilon$, the i–V characteristics for $eV < 2\varepsilon$ can be complicated and can exhibit hysteresis.

Inverse AC Josephson Effect. The *inverse* ac Josephson effect is observed when either incident RF radiation or an applied RF current of frequency f causes a dc voltage $V = hf/2e$ to appear across an unbiased junction. The junction can thus serve as a very sensitive detector of radiation. The i–V characteristic in this case exhibits current steps or spikes as a function of the voltage, with the voltage separation between steps given by $\Delta V = hf/2e$. For this application the use of a weak link in the form of a constriction or point contact is preferred due to the ease of coupling the radiation into or out of the junction.

Macroscopic Quantum Effects. The application of a transverse magnetic field H to a "short" S_1–I–S_2 Josephson junction can result in the flow of a tunneling current given by

$$J(\Phi) = J_c \sin\theta_0 \frac{\sin(\pi\Phi/\Phi_0)}{\pi\Phi/\Phi_0}. \tag{W16.17}$$

Here Φ is the total magnetic flux passing through the junction and given by $\Phi = BA_{\text{eff}} = \mu_0 H d_{\text{eff}} w$, Φ_0 is the quantum of flux, and θ_0 is the phase difference at a certain point in the junction. A "short" junction is defined as one for which the magnetic field of the junction current J is much less than the applied magnetic field H. Note that the effective junction width $d_{\text{eff}} = (d + \lambda_1 + \lambda_2)$ accounts for the penetration of magnetic flux into the two superconductors adjacent to the junction (see Fig. W16.14). This current represents a *macroscopic quantum interference effect* in which $J(\Phi)$ oscillates as a function of the magnetic flux Φ passing through the effective area A_{eff} of the junction. Note that $J = 0$ when $\Phi = n\Phi_0$ (i.e., whenever an integral number of flux

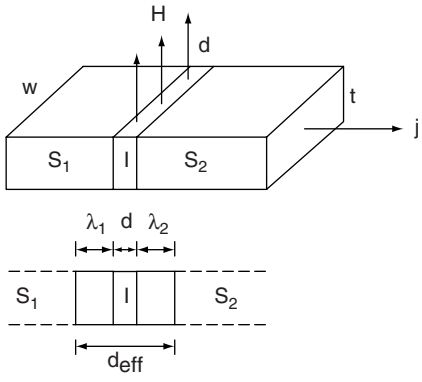

Figure W16.14. Application of a magnetic field H to an S_1–I–S_2 tunnel junction results in magnetic flux $\Phi = BA_{\text{eff}}$ passing through the junction.

quanta pass through A_{eff}). The actual current flow changes directions over the cross section of the junction perpendicular to the direction of the current flow.

W16.11 SQUIDS and Other Small-Scale Applications

The sensitivity of the two-junction loop (see Fig. 16.23*a*) to changes in magnetic flux can be illustrated by first noting that the total change in phase $\Delta\theta$ of the superconducting order parameter around the loop is proportional to the total magnetic flux Φ passing through the loop. This follows from the expression

$$\oint \nabla\theta \cdot d\mathbf{l} = \frac{2\pi}{\Phi_0} \oint \mathbf{A} \cdot d\mathbf{l}, \tag{W16.18}$$

where $\mathbf{A}$ is the vector potential and the integrals are taken around the loop along a path on which the current density $J = 0$. The integral on the left is equal to $\Delta\theta$ while the integral on the right is just the total flux Φ. Evaluation of the two integrals therefore yields

$$\Delta\theta = \theta_a - \theta_b = \frac{2\pi\Phi}{\Phi_0}, \tag{W16.19}$$

assuming that the loop currents do not contribute to the flux Φ. Since the phase is constant within each superconductor, the changes in phase θ_a and θ_b occur across the respective junctions.

The total current i passing through the two-junction loop from an external source is given by the sum of the individual currents passing through each junction, which can be written using Eqs. (W16.13) and (W16.19) as

$$\begin{aligned} i &= i_a(\theta_a) + i_b(\theta_b) = i_{ca}\sin\theta_a + i_{cb}\sin\theta_b \\ &= i_{ca}\sin\theta_a + i_{cb}\sin\left(\theta_a - \frac{2\pi\Phi}{\Phi_0}\right) = i(\Phi). \end{aligned} \tag{W16.20}$$

For the idealized case where the two junctions carry equal currents $i_{ca} = i_{cb} = i_c$, it can be shown that the maximum current that can flow depends on the flux Φ through

the loop and is given by

$$i_{\max}(\Phi) = 2i_c \left| \cos \frac{\pi \Phi}{\Phi_0} \right| . \tag{W16.21}$$

This is known as the *Josephson loop interference equation* since, in the absence of an applied voltage, no net current i can flow through the loop when the total flux through the loop $\Phi = (n + \frac{1}{2})\Phi_0$ due to destructive interference between the two Josephson currents i_a and i_b. The existence of these interference effects justifies calling the loop containing two Josephson junctions a *superconducting quantum interference device* (i.e., a SQUID). In practice the two junctions in the loop will not be identical, so the resulting, more complicated expression for $i(\Phi)$ will depend on both i_{ca} and i_{cb}. Also, when the magnetic flux passing through the junctions cannot be neglected, the current i given in Eq. (W16.20) will be modulated due to the quantization of flux within the junctions themselves.

From a practical point of view, the fabrication of SQUIDs from high-T_c superconductors that can operate at $T = 77$ K is a significant challenge, due to the necessity of maintaining bulk superconducting properties up to within a coherence length ξ of the junction interface. This will be difficult even in the *ab* plane, where $\xi_{ab} \approx 1.5{-}2$ nm. Fortunately, grain boundaries making high angles with respect to the CuO_2 layers that occur naturally in $YBa_2Cu_3O_7$ or which can be introduced during growth can act as Josephson junctions. A significant disadvantage of operating a SQUID at $T = 77$ K is the higher thermal noise that results in loss of resolution when compared to operation at $T = 4.2$ K.

SQUIDs have been used for sensitive electrical and magnetic measurements in the following configurations, shown in Fig. 16.23:

1. In the SQUID-based picovoltmeter the voltage is converted into a change of magnetic flux to which the SQUID can respond.
2. The SQUID magnetometer consists of a dc SQUID (i.e., a pair of Josephson junctions) coupled magnetically to a larger pickup loop. A resolution in magnetic flux density B of 10^{-15} T can be achieved. This corresponds to approximately $10^{-4}\Phi_0$ over an area of 10^{-4} m^2.

Some additional small-scale applications of superconductors are outlined briefly next.

Superconducting Computer Devices. The ability of Josephson junctions to switch from the superconducting to the normal state and back within a few picoseconds (i.e., at frequencies ≈ 100 GHz) with very low power dissipation makes possible their use in ultrafast superconducting digital devices, including logic circuits, shift registers, and A/D converters. These devices will probably make use of either single flux-quantum (SFQ) logic or single-electron logic (SEL). The demonstrated compatibility of junction fabrication with Si-based processing technology will be important for this application. An important advantage of low-temperature operation, at either $T = 4.2$ or 77 K, will be the stability of the devices with respect to the phenomenon of electromigration, which is a serious problem for semiconductor devices operated at room temperature and above.

Optical Detectors. The rapid change in resistivity observed near T_c means that the resistance of a superconductor which also has a low heat capacity can be very sensitive to outside sources of energy. Thin-film superconducting devices based on this effect,

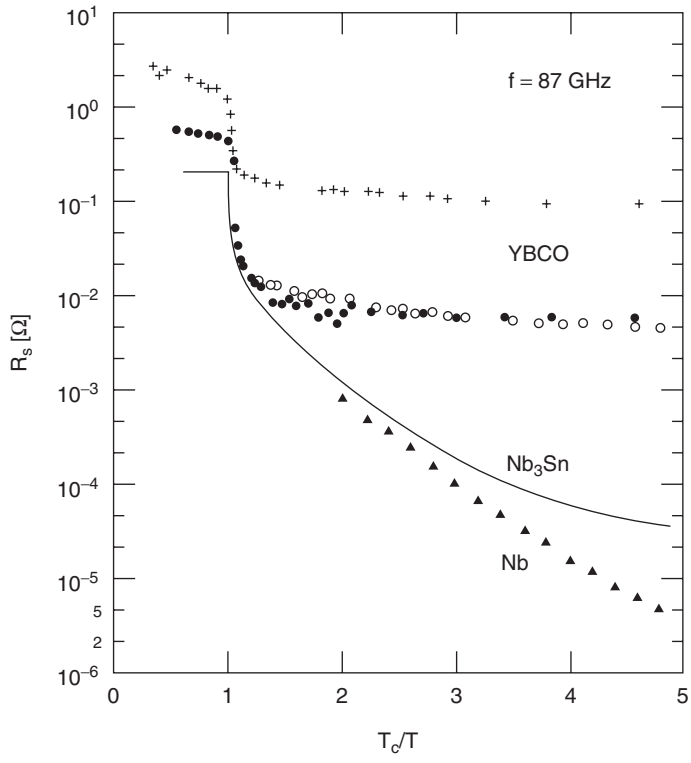

Figure W16.15. Temperature dependence of the measured microwave surface resistance R_s for the high-T_c superconductor $YBa_2Cu_3O_7$ is compared with other superconductors. [From H. Piel and G. Mueller, *IEEE Trans. Magn.*, **27**, 854 (1991). Copyright 1991 IEEE.]

known as *transition-edge bolometers*, have been employed as sensitive detectors of far-infrared radiation. SIS tunnel junctions can also function as sensitive detectors of single photons at infrared frequencies. A photon absorbed in the superconducting thin film breaks superconducting Cooper pairs, thereby generating a cascade of electrons that tunnel through the junction. The total charge collected is proportional to the energy of the incident photon.

Thermal Switches. Superconducting wires with very low κ_s/κ_n ratios of thermal conductivities in the superconducting and normal states are often used as thermal switches. For example, a Pb wire at $T = 4.2$ K has $\kappa_s/\kappa_n \approx 1/100$ and a critical field $H_C \approx 6.4 \times 10^4$ A/m (≈ 800 G). Thus for $H < H_C$ a thin Pb wire in the superconducting state will serve as a thermal insulator. When a field $H > H_c$ is applied, the Pb wire will serve as a good conductor of heat. This capability has been used in cryogenic heat capacity measurements where the sample being studied can be placed in good contact with a liquid He bath and then thermally isolated simply by switching the magnetic field applied to the Pb wire from $H > H_c$ to $H < H_c$.

Microwave Components and Devices. The uses of thin films of the high-T_c superconductor $YBa_2Cu_3O_7$ or the conventional superconductor Nb as delay lines, resonators, and filters in passive microwave devices are being developed due to the

accompanying reduction of losses resulting from the low microwave surface resistances R_s of these materials. For example, epitaxial thin films of $YBa_2Cu_3O_7$ have much lower values of R_s at $T = 77$ K for frequencies up to 100 GHz than are found in normal metals such as Cu and Au. Measured values of R_s for $YBa_2Cu_3O_7$ as a function of temperature are compared with other superconductors in Fig. W16.15. For successful operation, the properties of the superconducting film must be uniform in the surface region corresponding to the penetration depth λ.

One important goal is the achievement of more communication channels in the microwave region of the electromagnetic spectrum for cellular and "personal communication" applications through the use of filters based on high-T_c thin films, which have sharper frequency cutoffs than Cu filters. These microwave devices are likely to be the first successful applications of the high-T_c superconductors.

REFERENCE

Hebard, A. F., Superconductivity in doped fullerenes, Phys. Today, Nov. 1992, p. 26.

PROBLEMS

W16.1 Using the Gibbs free energy per unit volume for the superconducting state as given by the two-fluid model in Eq. (W16.1), calculate (**a**) $C_s(T)$ as $T \to 0$, and (**b**) $\Delta C(T_c) = C_n(T_c) - C_s(T_c)$.

W16.2 A magnetic field H is applied parallel to the surface of a long superconducting cylinder. (*Note*: See Fig. 16.10.)

- **(a)** Show that the variation of the effective magnetization M_y [$= (B_y/\mu_0) - H_y$] resulting from the supercurrents near the surface of the superconductor is given by $M_y(x) = -H_y(x = 0)(1 - e^{-x/\lambda_L})$.
- **(b)** What is the resulting value of M_y inside the superconductor (i.e., for $x \gg \lambda_L$)?

W16.3 A superconducting wire of radius $a = 1$ mm is formed into a single-turn circular loop of radius $r = 10$ cm. A current i is observed to flow around this isolated loop for five years without any measurable decay. Estimate a lower limit for the electrical conductivity σ (or an upper limit for the resistivity ρ) of this wire in the superconducting state. (*Hint*: The inductance of a single-turn circular loop of wire is $L \approx \mu_0 r[\ln(8r/a) - 2]$.)

W16.4 A type I superconductor has a critical magnetic field slope at $T_c = 3$ K given by $d(\mu_0 H_c)/dT = -15$ mT/K.

- **(a)** Estimate its critical field H_{c0} at $T = 0$ K. [*Hint*: Make use of the parabolic expression for $H_c(T)$ given in Eq. (16.6).]
- **(b)** Estimate the superconducting condensation energy per unit volume $G_n - G_s$ at $T = 0$ K for this superconductor.

W16.5 Show that the parabolic dependence of $H_c(T)$ given in Eq. (16.6) follows from the two-fluid expression for $G_s(T)$ of Eq. (W16.1) when the temperature dependence of the fraction of superconducting electrons is given by $f_s(T) = 1 - (T/T_c)^4$.

W16.6 For the A15 structure shown in Fig. W16.2 with the chemical formula Nb_3Ge and cubic lattice constant $a = 0.515$ nm, write down the NN and second-NN configurations and distances for both the Nb and Ge atoms.

W16.7 In the superconducting oxide $Ba_{1-x}K_xBiO_{3-y}$ with the cubic perovskite crystal structure, oxygen vacancies can be present to provide ionic charge compensation for the replacement of Ba^{2+} ions by K^+ ions. What value of y would be needed for complete ionic charge compensation of this material when $x = 0.4$?

W16.8 Show that the $n = 0$, 1, and 2 versions of the $HgBa_2Ca_nCu_{n+1}O_{(2n+4)+x}$ compound with $x = 0.06$, 0.22, and 0.40 have 0.12, 0.22, and 0.27 holes per Cu atom, respectively. The additional oxygen atoms can be assumed to have entered the Hg^{2+} layers.

W16.9 **(a)** Using the results that the penetration depth $\lambda \propto (m^*)^{1/2}$ and the coherence length $\xi \propto (m^*)^{-1/2}$, show that the inequalities $\xi_{ab} > \xi_c$ and $\lambda_c > \lambda_{ab}$ apply to anisotropic superconductors in which $m_c^* \gg m_a^* = m_b^*$.

(b) Using $H_{c2}(i) = \Phi_0/2\sqrt{2}\mu_0\xi_j\xi_k$, show that $H_{c2}(ab)/H_{c2}(c) = \sqrt{m_c^*/m_{ab}^*}$.

W16.10 Show that the expression $J_c(T) = H_c(T)/\lambda(T)$ for the critical transport current density can be derived by setting the kinetic energy density KE/V of the supercurrents equal to the superconducting condensation energy per unit volume $\mu_0 H_c(T)^2/2$. [*Hint*: Use $\text{KE}/V = (n_s/2)(2m)\langle v\rangle^2/2$, where $\langle v\rangle$ is defined by $J_c = (n_s/2)(2e)\langle v\rangle$ for the Cooper pair current.]

W16.11 Starting from Eqs. (W16.8) and (W16.9), derive the Josephson relations given in Eqs. (W16.11) and (W16.13).

W16.12 Sketch the tunneling current

$$J(\Phi) = J_c \sin\theta_0 \frac{\sin(\pi\Phi/\Phi_0)}{\pi\Phi/\Phi_0}$$

passing through the tunnel junction shown in Fig. W16.14 as a function of Φ/Φ_0. Note that $J = 0$ when $\Phi = n\Phi_0$ (i.e., whenever an integral number of flux quanta pass through the junction area A). Show that $J(\Phi \to 0)$ approaches the finite limit $J_c \sin\theta_0$.

W16.13 Consider a Nb–I–Pb junction which is $d = 50$ nm thick and 20 μm wide. For what value of magnetic field H applied perpendicular to the junction will exactly one quantum of flux Φ_0 be present within the effective area A_{eff} of the junction? Be sure to use the effective width of the junction $d_{\text{eff}} = d + \lambda_{Nb} + \lambda_{Pb}$ (see Fig. W16.14).